A General Reduced Order Model to Design and Operate Synthetic Jet Actuators

Tim Persoons[1]
University of Dublin, Trinity College, Dublin 2, Ireland

Synthetic jets are used in various applications from flow control to thermal management of electronics. Controlling the jet operating point using a simple voltage to velocity calibration becomes unreliable in case of external pressure field disturbances or varying actuator characteristics. This paper presents a general lumped parameter model for a synthetic jet actuator with electromagnetic or piezoelectric driver. The fluidic model accurately predicts the synthetic jet operating point (i.e. Reynolds number and stroke length) based on the measured cavity pressure. The model requires only two empirical coefficients characterizing nozzle fluid damping and inertia. These can be obtained via calibration or estimated from pressure loss correlations and the governing acoustic radiation impedance. The model has been validated experimentally for a circular and rectangular orifice. The effect of nozzle damping on the nonlinear system response is discussed. Analytical expressions are given for the two resonance frequencies characterizing the system response, as a function of the diaphragm and Helmholtz resonance frequencies. The optimal design of an impinging synthetic jet actuator is discussed in terms of the thermal and acoustic efficiency. Guidelines for selecting the optimum combination of diaphragm and Helmholtz resonance frequency are presented and compared to previous studies.

Nomenclature

A	=	cross-sectional area (m^2)
a	=	radius (m)
Bl	=	electromagnetic force factor (Tm)
C	=	damping coefficient (Ns/m) or capacitance (F)

[1] Marie Curie-IRCSET Fellow, Department of Mechanical and Manufacturing Engineering, Trinity College, Dublin 2, Ireland. Present address: School of Mechanical Engineering, Purdue University, 585 Purdue Mall, West Lafayette IN, 47907, USA (Tel.: +1 765 494 5638, Fax: +1 765 494 0539, E-mail: timpersoons@purdue.edu).

c = speed of sound (m/s)

d = hydraulic diameter (m)

e = voltage (V)

F = force (N)

i = current (A)

j = imaginary unit ($(-1)^{1/2}$)

K = stiffness (N/m)

k = wave number ($2\pi f/c$) (m^{-1})

M = mass (kg)

f = frequency (Hz)

L = length (m) or inductance (H)

P = power (W)

p = pressure (relative to ambient) (Pa)

R = resistance (Ω)

r = distance from source (m)

s = Laplace variable ($j\omega$) (s^{-1})

U = velocity (m/s)

x = position (m)

Z = impedance, acoustic (Ns/m) or electrical (Ω)

Greek symbols

ζ = critical damping ratio

μ = dynamic viscosity (Ns/m^2)

ν = kinematic viscosity (m^2/s)

ρ = density (kg/m^3)

ω = angular velocity ($2\pi f$) (rad/s)

Subscripts

0 = back side of component or jet characteristic

1 = front side of component

A = acoustic

a = ambient

c = cavity

d = diaphragm

e = electrical

f = fluid

H = Helmholtz resonance

n = nozzle

T = thermal

I. Introduction

A synthetic jet consists of a train of vortices that form by successive ejection and suction of fluid across an orifice, creating a directional flow without net mass input yet with a non-zero momentum flux. The flow is driven by periodic pressure variations generated in a cavity with a movable diaphragm. A free axisymmetric synthetic jet flow is characterized by two parameters: the stroke length L_0/d and the Reynolds number $Re = U_0 d/\nu$, where d is the nozzle hydraulic diameter and $U_0 = L_0 f$. The stroke length L_0 is the average distance traveled by fluid ejected during one half period or $L_0 = \int_{t=0}^{1/(2f)} U(t)dt$, where $U(t)$ is the area-averaged orifice velocity [1,2]. The dimensionless stroke length L_0/d is the inverse of a Strouhal number ($L_0/d = \left(fd/U_0\right)^{-1}$) and determines the flow characteristics especially at low values of L_0/d. Based on an analytical derivation [3], no vortex detaches from an axisymmetric sharp-edged orifice unless $L_0/d > 0.5$. The threshold value is geometry dependent, e.g. for a two-dimensional sharp-edged orifice $L_0/d > \pi$ [3], with even higher values reported for a rounded edge [4,5]. It is well understood that L_0/d and Re are the main parameters governing a synthetic jet flow [2].

Controlling the synthetic jet operating point therefore requires knowledge of the jet velocity. This cannot be conveniently measured in industrial applications, and requires advanced methods such as laser-Doppler anemometry, particle image velocimetry or hot-wire anemometry. Typically a calibration is performed to determine the relationship between excitation voltage and jet velocity. However, this relationship is subject to actuator degradation and other external influences. To overcome this problem, a calibration of cavity pressure versus velocity is recommended instead [1,6,7].

Smith and Glezer [1] use a synthetic jet to deflect a primary stationary jet, and also characterized the synthetic jet with a pressure-velocity calibration, recording several calibration curves for different frequencies. For a pair of adjacent synthetic jets, Smith and Glezer [6] observed that the velocity is influenced by the presence of the adjacent jet, and therefore recommend a pressure-velocity calibration. Persoons et al. [8,9] studied the heat transfer characteristics of a pair of adjacent impinging synthetic jets. Due to the interfering pressure fields, a pressure-velocity calibration [7] is needed to maintain a constant Reynolds number when operating the jets at different phases.

Crittenden and Glezer [10] describe a compressible flow synthetic jet based on a piston-crank arrangement, characterizing the jet performance with cavity pressure measurements. A numerical quasi-static model is solved to predict the pressure-velocity relation, assuming adiabatic state changes in the cavity and one-dimensional compressible isentropic flow in the orifice, neglecting friction and additional losses. The model agrees satisfactorily with measured pressure data.

Lockerby and Carpenter [11] propose a computational approach for predicting the pressure-velocity relationship for micro-scale synthetic jets. Their numerical model assumes isothermal state changes in the cavity and laminar fully developed compressible flow in the orifice. Rathnasingham and Breuer [12] propose a simple analytical model similar to the one used in this paper, except their model assumes inviscid orifice flow without losses, satisfying the Bernoulli principle. These models [10-12] have a limited validity by not accounting for realistic nozzle damping, as shown in Sect. III.B.

McCormick [13] and Gallas et al. [14] present lumped parameter models for a synthetic jet actuator with loudspeaker and piezoelectric actuator respectively, in order to predict the jet velocity from the excitation voltage. The model by Gallas et al. [14] accounts for nonlinear nozzle damping, yet its effect on the results is not explicitly shown. Based on this model, Oyarzun and Cattafesta [15] used numerical techniques to optimize the response of a synthetic jet actuator, providing experimental validation of the optimized designs. Their results demonstrate that the nozzle dynamics must be well understood to achieve accurate results.

Kordik et al. [16] use a similar two-mass lumped parameter model to predict the system resonance frequencies of a synthetic jet actuator. Two resonances are identified which depend on the Helmholtz and diaphragm resonance frequencies, which was also found by Gallas et al. [14] and is confirmed in the present study (Eq. (26)). Although not considering nozzle damping, Kordik et al. [16] report a good agreement with experimental data.

Kooijman and Ouweltjes [17] present a lumped parameter model with nonlinear nozzle damping, to predict the jet momentum flux and sound radiation. The model is solved numerically in the time domain using a finite difference method, which allows for simulating non-harmonic excitation signals. A good agreement with experimental data is achieved only using the nonlinear damping model. Unfortunately since the results are limited to a single amplitude, the effect of nonlinear nozzle damping is not discussed at length.

Some studies use more advanced numerical techniques to derive reduced order models for synthetic jet actuators and their interaction with boundary layer flows. Redionitis et al. [18] used proper orthogonal decomposition to

extract a reduced order model based on computational fluid dynamics simulations and experimental data obtained using particle image velocimetry. The study provides some useful insights but is limited to a small range of operating conditions. While intrinsically embedded in the data analysis, the effect of orifice damping and inertia has not been singled out. Yamaleev and Carpenter [19] used the one-dimensional Euler equations to obtain a quasi one-dimensional model to characterize the behavior of synthetic jet actuators with a more complicated three-dimensional geometry. Their results are validated against experimental data and full Navier-Stokes simulations. The proposed quasi one-dimensional model predicts the behavior reasonably well for the chosen test cases, yet the nonlinearity of the system has not been discussed in detail. Filz et al. [20] propose neural networks to predict the interaction of a synthetic jet actuator with an orifice set at an oblique angle to the cross-stream boundary layer. Also for applications in feedback flow control, Kim et al. [21] use system identification methods to develop a dynamic model of a synthetic jet.

These studies [18-21] address the issue of interaction between a synthetic jet and a boundary layer, which is beyond the scope of the present study. For a comprehensive review of reduced order models for synthetic jets in quiescent flow, the reader is referred to Raju et al. [22]. However, none of these studies have clearly illustrated the effect of nozzle damping on the system response.

Therefore, this paper aims to establish a general lumped parameter model for a synthetic jet actuator operating in quiescent flow, and experimentally validate it for a circular and rectangular orifice. Since the nozzle flow dynamics are crucial in obtaining accurate results [15], this paper will pay specific attention to the effect of nozzle damping on the system response. As part of the overall model, the fluidic model enables robust control over the synthetic jet operating point (i.e. Reynolds number and stroke length), independent of external influences (e.g. varying electromechanical characteristics or interfering pressure fields). The model parameters should be easily obtained from geometric, material and electromechanical properties. Furthermore, the model should require only a limited number of empirical coefficients, which are determined via calibration or estimated from correlations or models.

II. Physical Model

This section describes a lumped parameter model of a synthetic jet actuator relating the electrical excitation to the synthetic jet velocity. The overall system response of a synthetic jet can be expressed as the transfer function below, representing the fluidic efficiency as the ratio of jet momentum flux to electrical input power:

$$\frac{\text{Fluidic power}}{\text{Electrical power}} \propto \frac{\rho A_n U_n^2 c}{e^2/Z_e} = \underbrace{\overbrace{\frac{\rho c U_n}{p_c}}^{\text{Operational model}} \frac{A_n U_n}{A_d U_d} \frac{p_c A_d}{U_d}}_{\text{Fluidic effects (cavity and nozzle)}} \cdot \underbrace{\left(\frac{U_d}{e}\right)^2 Z_e}_{\text{Electromechanical dynamics}} \tag{1}$$

where each variable corresponds to the lumped element indicated by the subscript (e.g. *n* for nozzle, *d* for diaphragm, *c* for cavity). A similar expression describes the thermal efficiency of an impinging synthetic jet (Sect. III.D).

Sections II.A and II.B discuss the coupling between the mechanical and fluidic model, and the effect of the electromechanical actuation. However these can be skipped without a loss of continuity. Section II.C describes the fluidic model $\rho c U_n / p_c$ proposed here to control the operation of a synthetic jet actuator.

A. Mechanical and Fluidic Model Coupling

Figure 1 indicates the relevant nomenclature for the diaphragm and synthetic jet actuator. The specifics of the motor (typically an electromagnetic or piezoelectric driver) are discussed in Sect. II.B. For the oscillating diaphragm, a lumped parameter approximation is valid up to the fundamental resonance frequency of the diaphragm. The effect of higher order vibration modes is not considered. The mechanical force balance of the diaphragm is

$$\left(M_d s^2 + C_d s + K_d\right) x_d = F_d - \left(p_{d,1} - p_{d,0}\right) A_d \tag{2}$$

where $s = j\omega$ is the Laplace variable, and M_d, C_d and K_d are the equivalent diaphragm mass, damping and stiffness. F_d is the force exerted by the motor on the diaphragm.

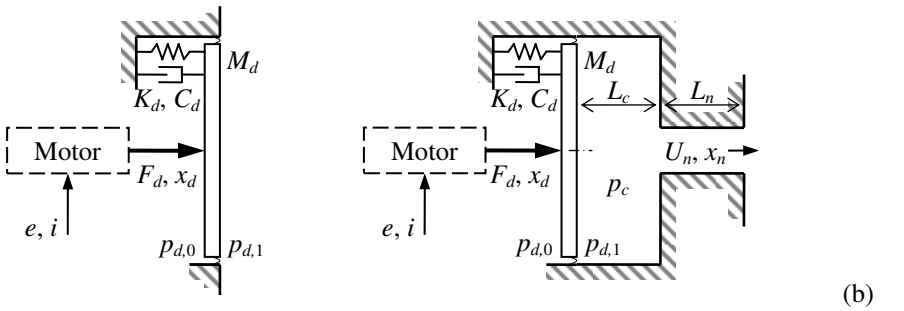

Fig. 1 Schematic diagram of an actuated diaphragm (a) mounted in an infinite baffle or (b) coupled to a cavity and nozzle in a synthetic jet actuator.

The pressure difference $p_{d,1} - p_{d,0}$ between front and back of the diaphragm is governed by acoustic pressure variations due to the motion in the surrounding fluid. These can be expressed as acoustic impedances:

$$\left(p_{d,1}-p_{d,0}\right)A_d=\left(Z_{d,1}+Z_{d,0}\right)x_d s+\Delta p_d A_d \tag{3}$$

where the stationary pressure difference Δp_d is neglected hereafter.

1. Acoustic Impedance for Radiation

For an oscillating diaphragm exposed to a free field (Fig. 1a), the radiation impedance Z_d acts as a pure inertia if $f<c\Big/\left(50A_d^{1/2}\right)$ (see App. A, Eq. (A3)) [23,24]. Table 1 lists typical values of the coefficient β determining the added fluid mass $M_f=\rho A_d\beta\left(4A_d/\pi\right)^{1/2}$ on a single side of an oscillating diaphragm.

Table 1 Added fluid mass coefficient β contributing to the acoustic radiation impedance (ka < 0.25) on a single side of an oscillating diaphragm in different boundary conditions ($\beta=M_f\Big/\left(\rho A\left(4A/\pi\right)^{1/2}\right)$ (see Eq. (A3)). Data adapted from [24,25].

	Circular plate [24]	Rectangular plate (aspect ratio 32) [25]
Infinite baffle (one side)	$\beta = 4/(3\pi) \cong 0.4244$	$\beta \cong 0.224$
Unflanged pipe (outer side)	$\beta \cong 0.307$	
Free mounted (1/2 of both sides)	$\beta \cong 0.212$	

Combining Eqs. (2,3) and neglecting Δp_d, the radiation can be lumped into an equivalent diaphragm mass:

$$\frac{x_d}{F_d}=\frac{1}{M_d' s^2+C_d s+K_d} \quad \text{where } M_d'=M_d+M_f \text{ according to Eq. (A3)} \tag{4}$$

2. Acoustic Impedance for Cavity and Nozzle

In a synthetic jet actuator, the diaphragm is coupled to a cavity (Fig. 1b). The influence of the diaphragm motion on the cavity pressure p_c can also be expressed as impedance $Z_c=p_c A_d/U_d$, to be substituted in place of $Z_{d,1}$ in Eq. (3). The conservation of mass in the cavity yields

$$\frac{\partial\left(\rho V_c\right)}{\partial t}=-\rho A_n U_n \quad \text{or} \quad \frac{1}{\rho c^2}\frac{\partial p_c}{\partial t}=\frac{A_n}{V_c}\left(\frac{A_d}{A_n}\frac{\partial x_d}{\partial t}-\frac{\partial x_n}{\partial t}\right) \tag{5}$$

where the speed of sound is defined as $c=\sqrt{\partial p/\partial\rho}$ assuming adiabatic state changes. The nozzle and cavity can be regarded as a pure acoustic mass oscillating against a pure compliance when the wavelength is much greater than the characteristic dimensions [24]. In terms of frequency,

$$f < \frac{1}{16}\frac{c}{\max\left(L_{c,\max}, L_{n,\max}\right)} \tag{6}$$

where $L_{c,max}$ and $L_{n,max}$ represent the largest linear dimensions of cavity and nozzle respectively. A geometric sensitivity study by Kordik et al. [16] shows that the behavior is dominated by the cavity volume, not its shape. Under these assumptions, the conservation of momentum in the nozzle yields

$$\underbrace{\rho A_n L_n \frac{\partial^2 x_n}{\partial t^2}}_{\text{inertia}} = -\underbrace{C_n U_n}_{\text{damping}} - \underbrace{\left(p_{n,1} - p_{n,0}\right) A_n}_{\text{driving pressure}} \tag{7}$$

where the damping force (C_nU_n) generally comprises both viscous friction and other pressure losses (e.g. boundary layer development, contraction and expansion losses) as discussed in Sect. II.C. The driving pressure in Eq. (7) is determined by the cavity pressure and the radiation impedance at the nozzle edges:

$$\left(\rho A_n L_n s^2 + \left(C_n + Z_{n,1} + Z_{n,0}\right) s\right) x_n = p_c A_n \tag{8}$$

Substituting the impedances $Z_{n,1}$ and $Z_{n,0}$ in Eq. (8) with their low frequency approximations for $f < c/\left(50 A_n^{1/2}\right)$ (see App. A) yields

$$\left(\rho A_n L_n' s^2 + C_n s\right) x_n = p_c A_n \text{ where } L_n' = L_n + 2\beta\sqrt{4A_n/\pi} \tag{9}$$

The added mass coefficient β (i.e. the average of $\beta_{n,0}$ and $\beta_{n,1}$ on both nozzle edges) can be estimated e.g. from Table 1, yet typically it should be determined via calibration. Substituting Eq. (9) into Eq. (5) yields the cavity impedance:

$$Z_c = \frac{p_c A_d}{U_d} = \left(\frac{A_d}{A_n}\right)^2 \frac{K_c\left(M_n' s^2 + C_n s\right)}{s\left(M_n' s^2 + C_n s + K_c\right)} \tag{10}$$

where $M_n' = \rho A_n L_n'$ and K_c represents the cavity stiffness $K_c = \rho c^2 A_n^2 / V_c$. The cavity acts as a driven Helmholtz resonator, with resonance frequency f_H

$$f_H = \frac{1}{2\pi}\sqrt{\frac{K_c}{M_n'}} = \frac{1}{2\pi}\frac{c}{L_n'}\sqrt{\frac{A_n L_n'}{V_v}} \tag{11}$$

The effect of the cavity is incorporated via Z_c in the diaphragm equation of motion (Eq. (2,3)):

$$\frac{x_d}{F_d} = \frac{1}{M_d s^2 + \left(C_d + Z_c + Z_{d,0}\right) s + K_d} \text{ with } Z_c \text{ according to Eq. (10)} \tag{12}$$

where $Z_{d,0}$ is the radiation impedance for the back of the diaphragm and $Z_{d,1}$ has been replaced by Z_c.

B. Electromechanical Actuation

Commonly used drivers for synthetic jet actuators are loudspeakers or piezoelectric membranes. Figure 2 depicts the equivalent circuits to model the response of both actuators.

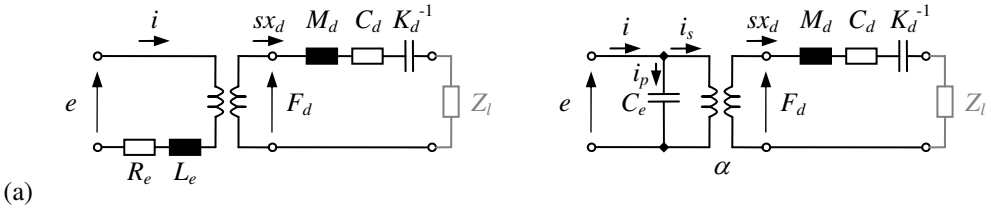

Fig. 2 Equivalent electrical circuits of (a) loudspeaker voice coil and (b) piezoelectric membrane, where Z_l comprises the combined diaphragm radiation and cavity impedance.

1. Loudspeaker Voice Coil

An electromagnetic coil exerts a force $F_d = Bl\, i$ on the diaphragm, where the current i is

$$i = \frac{e - \Delta e_{emf}}{R_e + L_e s} = \frac{e - Bl\, x_d s}{R_e + L_e s} \tag{13}$$

Combining $F_d = Bl\, i$ with Eqs. (12,13) yields the electrical impedance:

$$Z_e = \frac{e}{i} = \underbrace{\left(R_e + L_e s\right)}_{\substack{\text{impedance for} \\ \text{rigid diaphragm}}} \frac{M_d s^2 + \left(C_d + Z_l\right) s + \left(K_d + K_{emf}\right)}{M_d s^2 + \left(C_d + Z_l\right) s + K_d} \text{ with } K_{emf} = \frac{\left(Bl\right)^2 s}{R_e + L_e s} \tag{14}$$

where the load impedance $Z_l = Z_c + Z_{d,0}$. Combining Eqs. (12,14) and $F_d / e = Bl / Z_e$ yields

$$\frac{x_d}{e} = \frac{1}{Bl\, s} \frac{K_{emf}}{M_d s^2 + \left(C_d + Z_l\right) s + \left(K_d + K_{emf}\right)} \tag{15}$$

Appendix B shows that this simple model accurately predicts the measured electrical impedance and sound pressure level (SPL) for the loudspeaker used in Sect. III. The peak impedance and SPL occur at the mechanical resonance frequency of the diaphragm:

$$f_d = \frac{1}{2\pi} \sqrt{\frac{K_d}{M_d'}} \tag{16}$$

where M_d' includes the added fluid mass due to acoustic radiation.

2. Piezoelectric Membrane

Commercial synthetic jet actuators use piezoelectric actuation because of their low mass and high electrical efficiency. Typically a planar extending piezoelectric element is fixed to a flexible substrate, thereby amplifying the displaced volume. The equivalent electrical circuit (Fig. 2b) consists of a parallel coupled electrostatic capacitance C_e and mechanical impedance, and is similar to the lumped parameter model by Gallas et al. [14]. The impedance represents membrane stiffness, inertia and damping, and depends on the materials and mounting. The electrical impedance and deflection are

$$Z_e = \frac{e}{i} = \underbrace{\left(C_p s\right)^{-1}}_{\substack{\text{impedance for} \\ \text{rigid diaphragm}}} \frac{M_d s^2 + \left(C_d + Z_l\right) s + K_d}{M_d s^2 + \left(C_d + Z_l\right) s + \left(K_d + \alpha^2 / C_e\right)} \text{ and}$$

$$\frac{x_d}{e} = \frac{i_s}{e} \frac{1}{\alpha s} = \frac{\alpha}{M_d s^2 + \left(C_d + Z_l\right) s + K_d} \tag{17}$$

where C_e is the electrostatic capacitance and α is proportional to the piezoelectric constant d_{31}, stiffness K_d and geometric parameters. The acoustic radiation in $Z_l \left(= Z_c + Z_{d,0}\right)$ can again be lumped into $M_d' = M_d + M_f$. Considering only the fundamental vibration mode, a piezoelectric driver has a resonance and anti-resonance frequency:

$$f_d = \frac{1}{2\pi} \sqrt{\frac{K_d}{M_d'}} \text{ and } f_{d,anti} = \frac{1}{2\pi} \sqrt{\frac{K_d + \alpha^2 / C_e}{M_d'}} \tag{18}$$

corresponding to a local minimum and maximum impedance, respectively.

C. Fluidic Model: Cavity Pressure to Nozzle Velocity

The transfer function of cavity pressure to nozzle velocity U_n / p_c can be obtained from the derivation in Sect. II.A. This pressure to velocity model is proposed here to control the operation of a synthetic jet actuator instead of a classic voltage to velocity (U_n / e) approach, which is subject to potential actuator degradation and other external influences.

Substituting Eq. (10) in Eq. (9) yields the ratio of diaphragm to nozzle volume velocity:

$$\frac{U_n}{U_d} \frac{A_n}{A_d} \left(= \frac{x_n}{x_d} \frac{A_n}{A_d} \right) = \left(\frac{A_n}{A_d} \right)^2 \frac{x_n}{p_c A_n} \underbrace{\frac{p_c A_d}{s x_d}}_{Z_c} s = \frac{K_c}{M_n' s^2 + C_n s + K_c} \tag{19}$$

Combining Eqs. (19,10), the transfer function of cavity pressure to nozzle velocity becomes

$$\frac{\rho c U_n}{p_c} = \rho c \frac{U_n}{U_d} \underbrace{\frac{U_d}{p_c A_d}}_{=Z_c^{-1}} A_d = \frac{\rho c A_n}{M_n' s + C_n} \tag{20}$$

The damping force ($C_n U_n$) can be modeled as a linear and quadratic term in U_n corresponding respectively to viscous friction and inertial pressure losses due to flow contraction and expansion and boundary layer development:

$$C_n U_n = \underbrace{fRe \frac{2\mu L_n}{d^2} A_n U_n}_{\substack{1^{st} \text{ order damping} \\ \text{(viscous friction)}}} + \underbrace{K A_n \frac{\rho |U_n|}{2} U_n}_{\substack{2^{nd} \text{ order damping} \\ \text{(inertial losses)}}} \tag{21}$$

where d is the nozzle hydraulic diameter and fRe is the product of Fanning friction factor and Reynolds number (e.g. $fRe = 16$ for fully developed laminar flow in a circular duct). In this oscillating flow fRe and K do not necessarily equal their respective stationary flow values and may contain multidimensional flow effects, so they should be determined via calibration [7] as described further in Sect. III.

Using numerical simulations, Raju et al. [26] studied the frequency dependence of the forces acting on the fluid in the nozzle. The viscous friction term is proportional to the Stokes number $\sqrt{\tfrac{1}{2}\pi f d^2/\nu}$ yet is normally very small. The inertial pressure loss term is constant up to a Stokes number of about 10, corresponding to a quasi-steady oscillatory flow regime [27]. At higher frequency, the nonlinear damping term decreases [26].

If viscous friction dominates (e.g. very long nozzle, or high viscosity) C_n becomes independent of U_n:

$$\frac{\rho c U_n}{p_c} \overset{\substack{1^{st} \text{ order} \\ \text{damping}}}{=} \sqrt{\frac{V_c}{A_n L_n'}} \frac{1}{s/\omega_H + 2\zeta} \tag{22}$$

where the Helmholtz frequency $\omega_H = (c/L_n')\sqrt{A_n L_n'/V_c}$ and the critical damping ratio $\zeta = fRe\left(2\mu L_n A_n/d^2\right)\big/\left(2M_n'\omega_H\right)$. Equation (22) corresponds to Eq. (6) in Persoons and O'Donovan [7]. However for short nozzles which are most common in synthetic jet actuators, the inertial losses dominate [26]. With a velocity-dependent damping coefficient $C_n = \tfrac{1}{2} K \rho A_n |U_n|$, the nonlinear transfer function becomes:

$$\frac{\rho c U_n}{p_c} \overset{\substack{2^{nd} \text{ order} \\ \text{damping}}}{=} \frac{\rho c A_n}{\rho A_n L_n' s + \frac{1}{2} K \rho A_n |U_n|} \tag{23}$$

Using the derivation in App. C, this is equivalent to

$$\left|\frac{\rho c U_n}{p_c}\right|^{\substack{2^{nd}\text{ order}\\ \text{damping}}} = \sqrt{\frac{2V_c}{A_n L_n'}}\,\frac{1}{\sqrt{\left(\frac{\omega}{\omega_H}\right)^2 + \sqrt{\left(\frac{\omega}{\omega_H}\right)^4 + K^2\left(\frac{V_c}{A_n L_n'}\right)^2\left(\frac{|p_c|}{\rho c^2}\right)^2}}} \tag{24}$$

$$\text{and } \phi_{U_n} - \phi_{p_c} = -\arctan\left(\frac{\omega/\omega_H}{\frac{1}{2}K|U_n|/(L_n'\omega_H)}\right)$$

This is the most appropriate model to control the operation of a synthetic jet actuator, and has proven successful in several studies using adjacent synthetic jets [8,9]. It is valid up to the geometry-dependent limit frequency defined by Eq. (6). Simple software tools to determine the empirical model coefficients K and β for Eq. (24) and evaluate the model are available from the author.

III. Experimental Validation

The model validation uses experimental data obtained with a loudspeaker-actuated synthetic jet, using two nozzle geometries. Section III.B focuses on the fluidic model (Eq. (24)) which uses the cavity pressure to predict the synthetic jet velocity. Sections III.C and III.D validate the electromechanical model and the overall system efficiency.

A. Experimental Approach

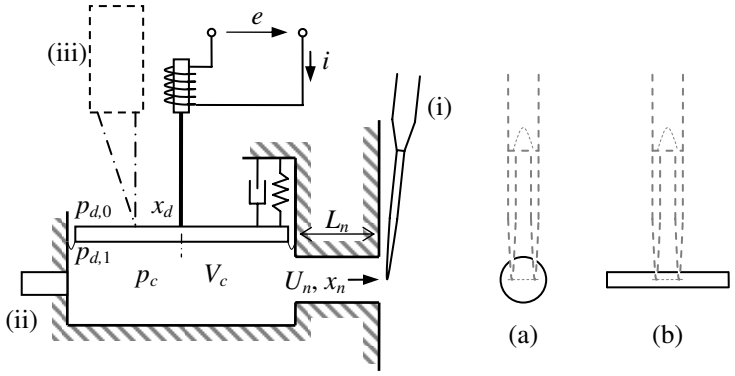

Fig. 3 Schematic diagram of instrumented synthetic jet actuator with (a) circular and (b) rectangular orifice (not to scale). Instrumentation includes (i) a hot-wire anemometer probe, (ii) cavity pressure microphone and (iii) laser displacement sensor.

Figure 3 shows a diagram of the synthetic jet actuator used to validate the model. The semi-cylindrical cavity (75mm diameter, $V_c = 113\,\text{cm}^3$) is machined from solid acrylic (PMMA). The top of the cavity consists of a

loudspeaker (Visaton FR8, 4Ω, 10W) driven by an audio amplifier (SoundLab G097, 90W, 100dB signal-to-noise ratio, total harmonic distortion <0.1%). The current i is measured using a shunt resistor (100mΩ, ±1%). Two interchangeable orifice plates are used ($L_n = 10$ mm) with a sharp-edged (a) circular orifice (5mm diameter) and (b) a 30:1 aspect ratio rectangular slot (1.5mm by 45mm in cross-section). The side-orifice layout (Fig. 3) facilitates measurements with two adjacent synthetic jets [8,9]. The orifice exit condition approximates an infinite baffle.

The jet velocity is measured using a hot-wire probe (Dantec 55P11, platinum-plated tungsten wire, 5μm diameter by 1.25mm long), operated in a constant temperature anemometer (Dantec 54T30, bridge ratio 20:1, resistance overheat ratio 1.8, 10kHz low pass filter). The probe is in line with the orifice center at 0.5mm (0.15d) from the orifice outlet to avoid velocity decay. For fully developed oscillating flow in a circular duct and a Stokes number $\sqrt{2fA_n/\nu}$ between 5 and 50, the area-averaged velocity U_n is 0.55 to 0.95 times the centerline velocity [14,27]. However L_n is much shorter than the minimum hydraulic development length (which exceeds 200mm), thus the measured centerline velocity is a reasonable estimate of U_n. The cross-flow position of the probe minimizes its flow disturbance. The calibration is performed in this position in a low turbulence wind tunnel against a pitot-static tube. A King's law relation is least-square fitted to the calibration points, resulting in an R^2 value of 99.9%.

The cavity pressure p_c is measured using a microphone (G.R.A.S. 40BD with 26CB CCP preamplifier, 1.6mV/Pa, 40-174dB, 4Hz-70kHz). The deflection of the loudspeaker diaphragm x_d is measured with a laser displacement sensor (Keyence LK-G157, range ±40mm, linearity ±0.05%) focused on the back of the speaker diaphragm. A National Instruments cDAQ-9178 data acquisition system with NI-9263 module generates the sine wave excitation for the speaker. All analog signals (e, i, U_n, p_c, x_d, ambient and jet temperature) are acquired using the same system with NI-9205 and NI-9213 modules, and are phase locked to the actuator excitation signal. For each operating point, the signals are phase-averaged over 10 periods to achieve an uncertainty level below 5% (based on a 95% confidence level) on the phase-averaged velocity and pressure waveforms.

B. Validation of the Fluidic Model (U_n/p_c)

Figure 4 shows the phase-resolved evolution of p_c, U_n and U_d within a single period for the synthetic jet with circular orifice, at four operating frequencies. The nozzle velocity is only shown during the ejection phase ($U_n > 0$) to avoid the directional ambiguity of hot-wire anemometry. Based on the measured cavity pressure magnitude

$\left|p_c^{(m)}\right|$, Eqs. (24,19) are used to predict the nozzle and diaphragm velocities U_n and U_d, represented by the dashed and dotted lines in Fig. 4. The measured velocities $U_n^{(m)}$ (●) and $U_d^{(m)}$ (○) are normalized to the magnitude predicted by Eqs. (24,19).

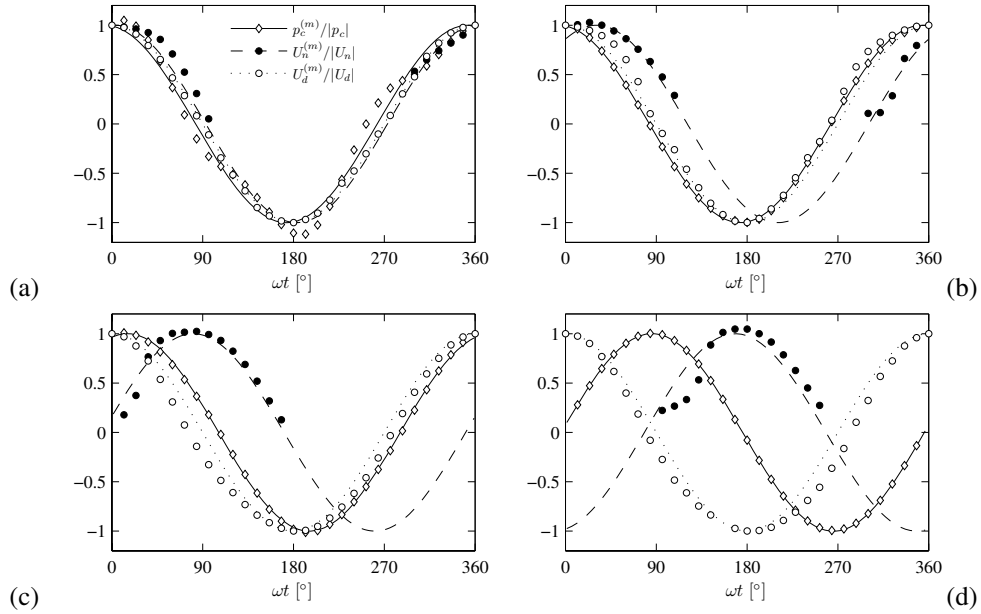

Fig. 4 Phase-resolved evolution of the normalised cavity pressure p_c (◇), nozzle velocity U_n (●) and diaphragm velocity U_d (○) (lines represent the model; markers represent experimental data) for a synthetic jet actuator with circular orifice at $|p_c|$ = 500Pa and (a) $f = 0.125f_H$, (b) $f = 0.5f_H$, (c) $f = f_H$, (d) $f = 2f_H$.

The agreement between measured and predicted velocity is very good, except for a small deviation at the start of the ejection phase. Well below the Helmholtz frequency ($f \ll f_H$) the pressure and both velocities are in phase (Fig. 4a). As the frequency increases, the phase lag between the nozzle and diaphragm velocity increases to 90° at resonance ($f = f_H$) and 180° for $f \geq 2f_H$. The phase lag between the nozzle velocity and cavity pressure rises from zero ($f \ll f_H$) to 90° for $f \geq 2f_H$.

While the data in Fig. 4 are obtained for a single cavity pressure magnitude ($\left|p_c\right| = 500$ Pa), similar measurements are taken for each orifice at a series of cavity pressures from 10Pa to 1000Pa and a range of frequencies $0.025 \leq f/f_H \leq 2$. Based on the measured ratio of $\left|U_n/p_c\right|$, the model in Eq. (24) is least-square fitted to the data. Persoons and O'Donovan [7] have shown that the linear damping model does not predict experimental

data very well. As such, the appropriate fitting parameters are (i) the nonlinear damping coefficient K and (ii) the added mass coefficient β.

Table 2 lists the least-square fitted parameters K and β for the two orifices used here. Although the quasi-steady flow regime is restricted to a low Stokes number ($\sqrt{\frac{1}{2}\pi f d^2/\nu} < 10$, or $f < 40$ Hz) [26,27], Persoons and O'Donovan [7] had already shown that the value of K is comparable to the pressure loss coefficient for steady flow through the nozzle, $\Delta p/\left(\rho U_n^2/2\right)$, comprising inertial losses such as contraction and expansion loss and boundary development. This is reconfirmed here by the pressure loss coefficients in Table 3 determined experimentally for the circular and rectangular nozzles, showing an average deviation of 13% between corresponding values in Tables 2 and 3. Values of K presented by Raju et al. [26] are about 50% of those in Tables 2 and 3, which could be partly due to geometric differences (e.g., fillets, cavity shape).

The least-square fitted values for β in Table 2 are about 30% higher compared to the values for infinite baffle conditions (Table 1) on both sides of the orifice. This discrepancy is likely because more fluid within the cavity is contributing to the added fluid mass in this particular configuration. For an orifice located in the wall directly opposite the diaphragm, the β value is closer to the infinite baffle value [7]. Similar to the theoretical values in Table 1, the rectangular slot has a lower added mass coefficient than the circular orifice.

Table 2 Model coefficients for both nozzles, obtained by fitting Eq. (24) to experimental data: (i) damping coefficient K and (ii) added mass coefficient $\beta = \frac{1}{2}\left(M_n' - M_n\right)/\left(\rho A_n\sqrt{4A_n/\pi}\right)$

	Circular orifice (R^2 = 99.8%)	Rectangular slot orifice (30:1) (R^2 = 99.5%)
Nonlinear damping coefficient K	1.251 (± 0.15)	1.552 (± 0.20)
Added mass coefficient β	1.039 (± 0.21)	0.615 (± 0.07)

Table 3 Pressure loss coefficient for steady flow through each nozzle $\Delta p/\left(\rho U_n^2/2\right)$ (to be compared to K values in Table 2)

	Circular orifice	Rectangular slot orifice (30:1)
Steady flow pressure loss $\Delta p/\left(\rho U_n^2/2\right)$	1.14 (± 0.12) (R^2 = 99.1%)	1.34 (± 0.14) (R^2 = 99.9%)

In summary, the estimates of K (based on the steady flow pressure loss; Table 3) and β (based on the acoustic radiation impedance; Table 1) are in reasonable agreement with the least-square fitted values in Table 2. Deviations of only 13% for K and 30% for β are remarkable considering the complex geometry and flow phenomena involved. As such, the model parameters K and β can be estimated with reasonable accuracy without needing a reference velocity measurement, yet for best accuracy experimental validation as described here is still recommended.

Figure 5 shows the comparison of the fluidic model U_n/p_c (Eq. (24) with K and β from Table 2) to experimental data obtained at a range of cavity pressures between 10 and 1000Pa. The upper graphs show the magnitude in decibel. The lower graphs show the phase angle, where negative values represent phase lag between numerator (U_n) and denominator (p_c). The agreement is excellent for the magnitude for frequencies up to the Helmholtz resonance. The uncertainty is higher for the phase angle although the trend is clear: near zero phase lag for $f \ll f_H$ and the phase lag between U_n and p_c approaches 90° for $f > 2f_H$.

For reference, the dashed lines in Fig. 5 represent the undamped model. In this hypothetical case, the nozzle fluid acts as an undamped acoustic mass and Eq. (20) reduces to $\rho c U_n/p_c = c/(L_n' s)$. This corresponds to the limit condition for high frequency or very low cavity pressure.

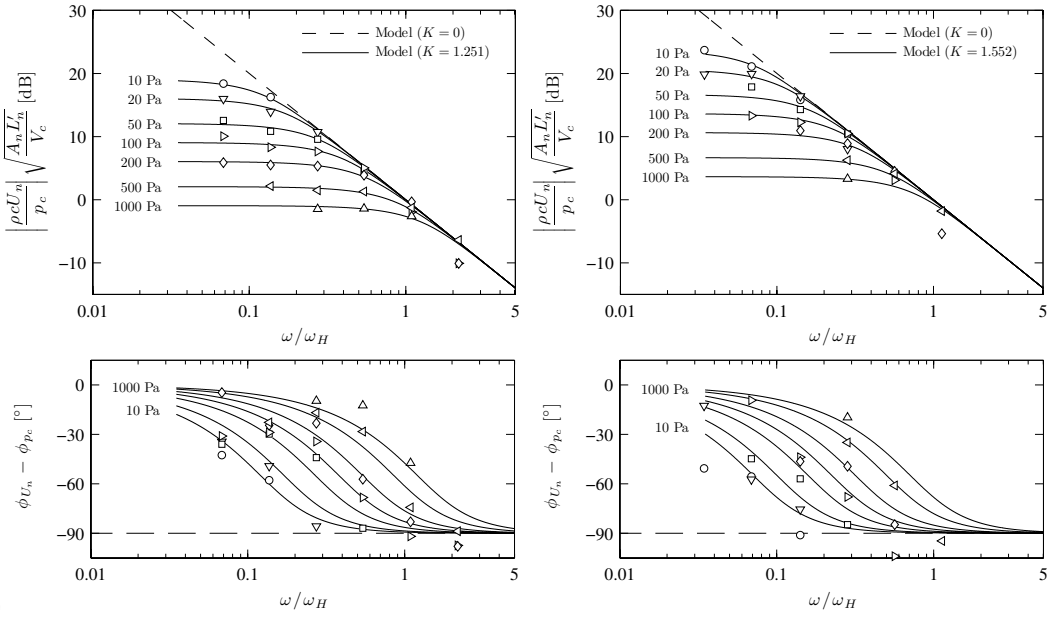

Fig. 5 Validation of the fluidic model U_n/p_c (Eq. (24) with K and β from Table 2) (lines) versus experimental data (markers) for a synthetic jet actuator with (a) circular and (b) rectangular orifice of aspect ratio 30:1. Markers represent cavity pressure magnitudes (○) 10Pa, (▽) 20Pa, (□) 50Pa, (▷) 100Pa, (◇) 200Pa, (◁) 500Pa, (△) 1000Pa.

The model in Eq. (24) can now be used to determine the Reynolds number and stroke length of the synthetic jet flow using only the cavity pressure measurement:

$$Re = \frac{\rho\left(|U_n|/\pi\right)\sqrt{4A_d/\pi}}{\mu} \text{ and } L_0 = \frac{|U_n|/\pi}{f} \text{ with}$$
$$|U_n| = \frac{|p_c|}{\rho c}\sqrt{\frac{2V_c}{A_n L_n'}}\frac{1}{\sqrt{\left(\frac{\omega}{\omega_H}\right)^2 + \sqrt{\left(\frac{\omega}{\omega_H}\right)^4 + K^2\left(\frac{V_c}{A_n L_n'}\right)^2\left(\frac{|p_c|}{\rho c^2}\right)^2}}} \tag{25}$$

where $\frac{1}{\pi}|U_n| = U_0$, the characteristic velocity for synthetic jets assuming sine wave excitation.

As discussed in Sect. II.A, the validity range is determined by the geometry-dependent limit frequency in Eq. (6), not by the Helmholtz resonance. For both actuators, the cavity diameter (75mm) determines the upper validity frequency (280Hz), or respectively 1.7 and 0.97 times the Helmholtz frequency for the circular and slot orifice.

The transfer function U_n/U_d (Eq. (19)) can also be validated using the measured rate of deflection of the diaphragm $\partial x_d/\partial t$. Figure 6 shows a reasonable agreement between the experimental data and the model. As in Fig. 5, the dashed curves represent the model without damping, which exhibits an unbounded response at the Helmholtz resonance frequency.

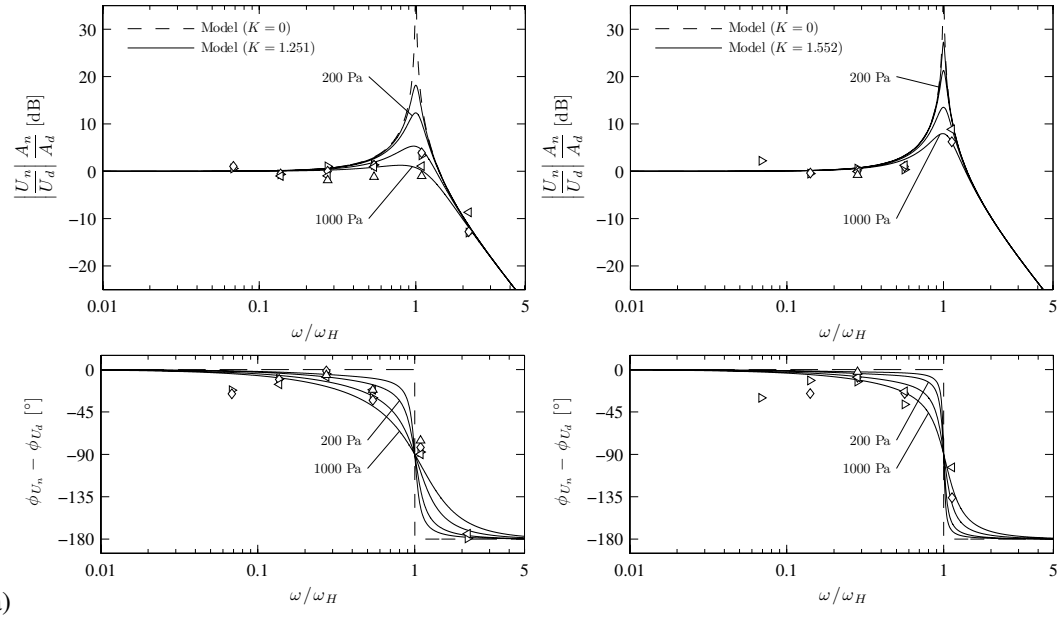

(a) (b)

Fig. 6 Transfer function U_n/U_d (Eq. (19) with K and β from Table 2) (lines) versus experimental data (markers) for a synthetic jet actuator with (a) circular and (b) rectangular orifice of aspect ratio 30:1. Markers represent cavity pressure magnitudes (▷) 100Pa, (◇) 200Pa, (◁) 500Pa, (△) 1000Pa.

C. Validation of the Electromechanical Model

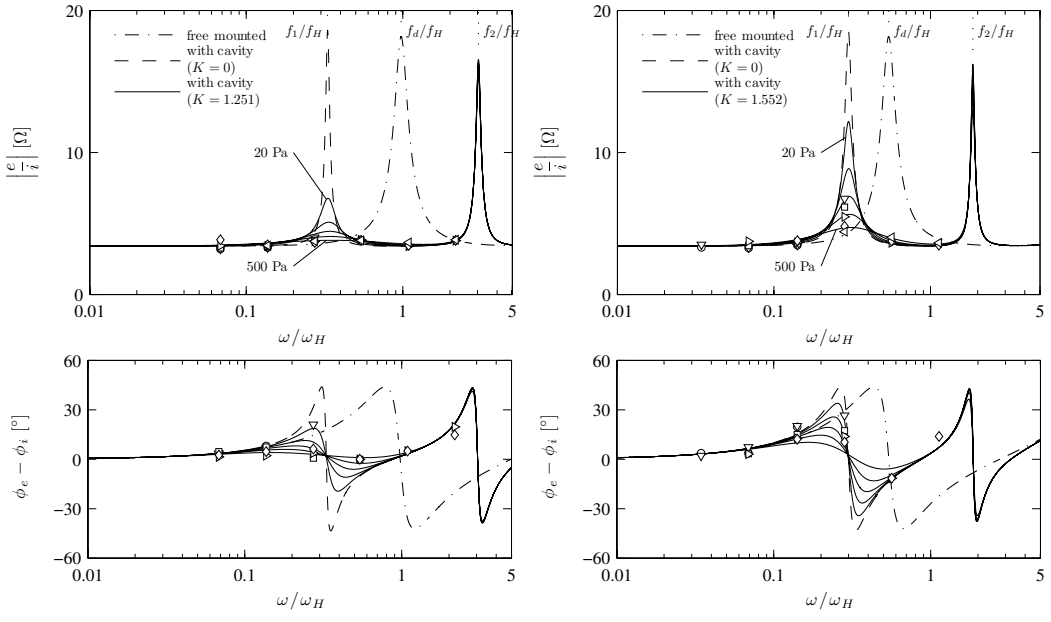

Fig. 7 Electrical impedance $Z_e = e/i$ (Eq. (14) with K and β from Table 2) (lines) versus experimental data (markers) for a synthetic jet actuator with (a) circular and (b) rectangular orifice of aspect ratio 30:1. Markers represent cavity pressure magnitudes (○) 10Pa, (▽) 20Pa, (□) 50Pa, (▷) 100Pa, (◇) 200Pa, (◁) 500Pa.

Figure 7 shows the electrical impedance of the loudspeaker mounted in the synthetic jet actuator. The experimental data are well predicted by Eq. (14) using the cavity impedance Z_c from Eq. (10) with K and β from Table 2. Similar to Figs. 5 and 6, the dashed lines represent the model without damping. The dash-dotted lines represent the electrical impedance of the free-mounted loudspeaker characterized by a single resonance peak at f_d (i.e. identical to Z_e curve in Fig. 13). Due to the presence of the cavity and nozzle, two resonance peaks appear at f_1 and f_2 which are determined by (but are not equal to) the Helmholtz frequency f_H (Eq. (11)) and the free diaphragm resonance f_d (Eq. (16) or (18)). Although the amplitude correspondence between the experimental markers and the lines representing the model may be difficult to evaluate, the phase angle shows a good agreement between experiments and model even at frequencies beyond f_H.

These two peak frequencies correspond approximately to the resonance frequencies of the mechanical diagrams in Fig. 8, and can be expressed as

$$f_1 \cong \frac{1}{2\pi}\sqrt{\frac{\left[K_c^{-1}+\left(\left(\frac{A_n}{A_d}\right)^2 K_d\right)^{-1}\right]^{-1}}{M_n'}} \quad \text{and} \quad f_2 \cong \frac{1}{2\pi}\sqrt{\frac{K_d+\left(\frac{A_d}{A_n}\right)^2 K_c}{M_d'}} \tag{26}$$

The lower frequency f_1 corresponds to a modified Helmholtz frequency, where the nozzle fluid is resonating against the cumulative compliance of the cavity K_c^{-1} and the diaphragm $\left(A_d/A_n\right)^2 K_d^{-1}$. The factor $\left(A_d/A_n\right)^2$ corrects for the different cross-sections in the equations of motion of the diaphragm and nozzle. The upper frequency f_2 corresponds to a modified diaphragm resonance frequency, where the diaphragm stiffness is augmented by the cavity stiffness. Figure 7 confirms that the nozzle damping (C_n) only affects the lower resonance peak at f_1.

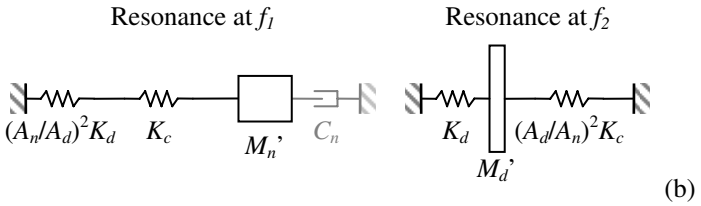

Fig. 8 Equivalent mechanical model of loudspeaker-driven synthetic jet actuator at lower and upper resonance frequencies (a) f_1 and (b) f_2 given by Eq. (26).

For a piezoelectric membrane actuator, Gallas et al. [14] report a similar behavior characterized by two resonance frequencies, and provide a quadratic equation to determine f_1 and f_2. Both Eq. (26) and the relation by Gallas et al. [14] give a good estimate of the peak frequencies in the system response, as will be shown in Sect. IV (Table 4). Similar findings are reported by other studies [16,17].

D. Validation of the Overall System Efficiency

1. Thermal Efficiency

In analogy to Silva and Ortega [28], the overall thermal efficiency of a synthetic jet-based cooling device is expressed as the ratio of its heat removal power P_T to the electrical input power P_e. Based on a recent study [29], the stagnation heat transfer rate in an impinging synthetic jet depends mainly on the jet Reynolds number ($P_T \propto Re^m \propto \left|U_n\right|^m$ where m varies between 0.7 and 0.9), and to a lesser extent on the stroke length $L_0 \propto \left|U_n\right|/f$. The heat transfer area affected by the jet depends on Re yet is relatively independent of L_0 [30]. Without loss of generality, the average heat transfer rate is approximately proportional to $\left|U_n\right|^2$. Similar to Eq. (1), the thermal efficiency can be written as

$$\frac{P_T}{P_e} \propto \frac{kL_{ref}^3 \Delta T}{\nu^2} \frac{U_n^2}{e^2} Z_e \tag{27}$$

For a given fluid and operating temperatures, the different jet designs and operating points can be compared using the following (arbitrarily scaled) thermal efficiency measure η_T:

$$\eta_T = \left(\frac{U_n}{U_d}\right)^2 \left(\frac{sx_d}{e}\right)^2 Z_e \tag{28}$$

Figure 9 shows $|\eta_T|$ as a function of frequency for the orifices used here. Although $|\eta_T|$ does not represent the true efficiency P_T/P_e, Fig. 9 does give useful information regarding the optimal operating frequency and amplitude.

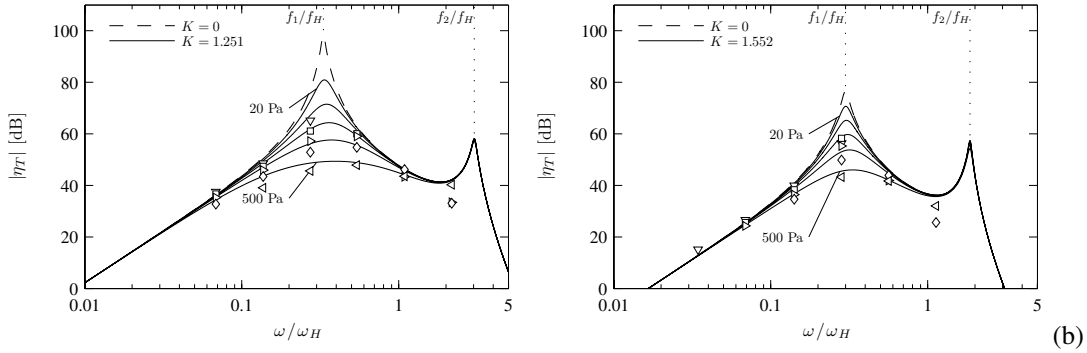

Fig. 9 Thermal efficiency η_T (Eq. (28) with K and β from Table 2) (lines) versus experimental data (markers) for a synthetic jet actuator with (a) circular and (b) rectangular orifice of aspect ratio 30:1. Markers represent cavity pressure magnitudes (▽) 20Pa, (□) 50Pa, (▷) 100Pa, (◇) 200Pa, (◁) 500Pa.

The frequencies f_1 and f_2 correspond to the peaks observed in the electrical impedance Z_e in Fig. 7 with nozzle damping affecting only the lower peak. Depending on the cavity pressure magnitude, maximum efficiency is achieved close to f_1 or f_2 defined by Eq. (26). Due to the nonlinear damping, operation at higher cavity pressure leads to stronger damping since $\zeta = C_n/(2\omega_H M_n') \propto K|p_c|$, which reduces the efficiency near f_1.

Using a piezoelectric synthetic jet actuator, Gallas et al. [14] also observed two resonance peaks in the system response, plotted as U_n at a constant excitation voltage e. At high enough cavity pressure, the lower peak can become hidden due to the nonlinear damping.

Using a loudspeaker actuator, Kooijman and Ouweltjes [17] present experimental and numerical results for the jet momentum flux at a fixed excitation voltage, which is proportional to $(U_n/e)^2$. Although they accurately model nonlinear nozzle damping, their validation is unfortunately limited to a single amplitude. Nevertheless, their results are qualitatively very similar to the efficiency plotted in Fig. 9. As above, two resonance peaks are observed, where only the lower peak is affected by nozzle damping.

2. Acoustic Efficiency

By analogy, the acoustic efficiency is defined as the ratio of emitted acoustic power $P_A \propto pUA$ to the electrical input power P_e. The emitted sound originates from the oscillating nozzle fluid slug as well as turbulence-generated noise. Considering only the nozzle fluid motion, the pressure near the orifice is determined by the radiation impedance $Z_n = pA_n/U_n$, therefore $P_A \propto Z_n U_n^2$. At low frequency $Z_n \cong M_f s$ (see Sect. II.A.1), and an acoustic efficiency measure η_A can be defined as

$$\eta_A = s\left(\frac{U_n}{U_d}\right)^2\left(\frac{sx_d}{e}\right)^2 Z_e \tag{29}$$

which is very similar to Eq. (28) and $\eta_A/\eta_T \propto f$. Optimal design of a synthetic jet cooler is achieved by maximizing thermal efficiency η_T while minimizing acoustic noise emission η_A.

In Fig. 9, although the thermal efficiency might be comparable for both resonance peaks at f_1 and f_2, the ratio of noise emission to heat removal power η_A/η_T increases with frequency. Here, this ratio is nearly an order of magnitude higher at the upper peak ($\cong f_2/f_1$), which would favor operation at the lower resonance peak f_1.

However, these expressions are based on rather crude assumptions, both for the thermal efficiency ($P_T \propto |U_n|^2$) and acoustic efficiency (e.g. neglecting turbulent noise, reflection and directivity, psychoacoustics). Acoustic sound emission experiments are beyond the scope of the present study, yet this will be investigated in a follow-up research.

IV. Discussion: Piezoelectric or Electromagnetic Actuation and Optimal Design

Commercial synthetic jet-based cooling devices use piezoelectric membrane actuators instead of loudspeakers, because of their lower mass and higher efficiency. However Sect. II.B has shown that the electrical impedance and deflection-to-voltage ratio (Eqs. (14,15,17)) have a similar functional form. For the synthetic jet actuator used here, Fig. 10 compares the electrical impedance of (i) the loudspeaker (grey lines) to (ii) an equivalent piezoelectric actuator (black lines) with the same diaphragm resonance frequency, area and mass.

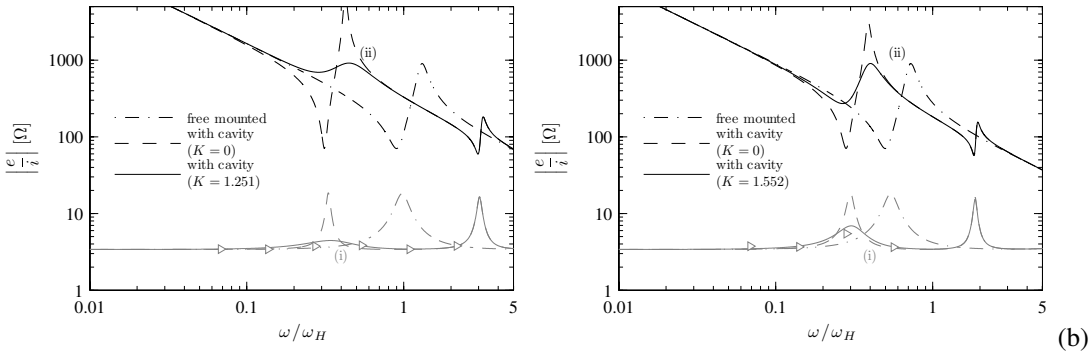

Fig. 10 Electrical impedance $Z_e = e/i$ for a synthetic jet actuator with (a) circular and (b) rectangular orifice of aspect ratio 30:1, using (i) a loudspeaker (Eq. (14)) and (ii) an equivalent piezoelectric membrane with the same resonance frequency (Eq. (17)). The measured data (▷) represent a cavity pressure magnitude of 100Pa.

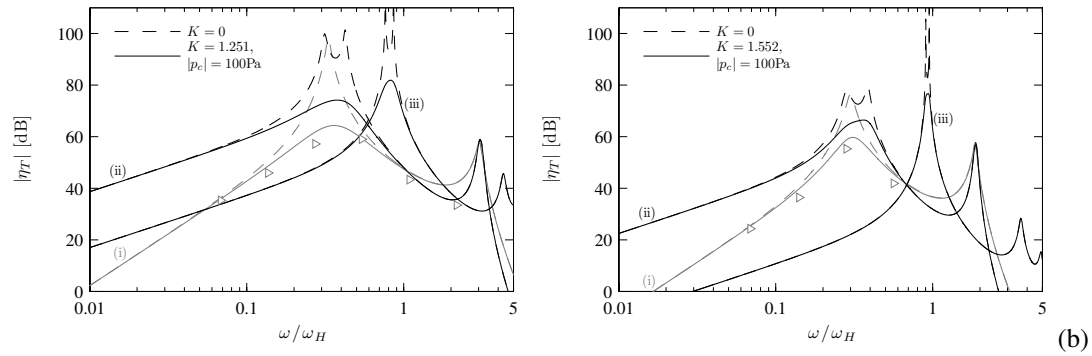

Fig. 11 Thermal efficiency η_T (Eq. (28) with K and β from Table 2) of a synthetic jet actuator with (a) circular and (b) rectangular orifice of aspect ratio 30:1, using (i) a loudspeaker and a piezoelectric membrane with (ii) the same resonance frequency and (iii) optimized for maximum thermal efficiency. The measured data (▷) represent a cavity pressure magnitude of 100Pa.

Figure 11 shows the thermal efficiency for the (i) loudspeaker and (ii) piezoelectrically actuated synthetic jet. The dashed lines represent the hypothetical undamped response, whereas the solid lines represent the actual damped response for a representative cavity pressure magnitude of 100Pa. The third set of curves in Fig. 11 represents (iii) an optimized piezoelectric actuator (coupled to the same cavity and nozzle), with a diaphragm resonance frequency that achieves maximum thermal efficiency at its lower resonance peak. Table 4 lists the resonance frequencies and peak efficiencies for the three cases in Fig. 11.

The diaphragm resonance frequency to achieve peak efficiency is $3.4f_H$ for both orifices (see Table 4). Figure 11 shows that the efficiency curve for actuator (iii) exhibits a much sharper peak. The gain in maximum efficiency between actuators (ii) and (iii) is about 2.2× and 3.5× for the circular and rectangular orifice respectively. While the actual efficiency magnitude is not important here, this analysis has shown that exactly matching the mechanical

diaphragm resonance frequency f_d to the Helmholtz frequency f_H does not yield the maximum thermal efficiency. Instead, peak efficiency is achieved when the system resonance frequency f_1 is close but not equal to f_H.

Table 4 Performance characteristics of synthetic jet actuator using (i) a loudspeaker and a piezoelectric membrane with (ii) the same resonance frequency and (iii) optimized for maximum thermal efficiency. (Values for f_1 and f_2 obtained from (a) Eq. (26), (b) Gallas et al. [14], (c) Fig. 11)

	Circular orifice (f_H = 161Hz)			Rectangular orifice (f_H = 290Hz)		
Type of actuator	(i)	(ii)	(iii)	(i)	(ii)	(iii)
Diaphragm resonance frequency f_d	$0.98f_H$	$0.98f_H$	$3.4f_H$	$0.54f_H$	$0.54f_H$	$3.4f_H$
System resonance frequency f_1	(a) $0.35f_H$ (b) $0.33f_H$ (c) $0.36f_H$	(a) $0.33f_H$ (b) $0.31f_H$ (c) $0.35f_H$	(a) $0.77f_H$ (b) $0.76f_H$ (c) $0.83f_H$	(a) $0.35f_H$ (b) $0.30f_H$ (c) $0.31f_H$	(a) $0.33f_H$ (b) $0.28f_H$ (c) $0.31f_H$	(a) $0.91f_H$ (b) $0.90f_H$ (c) $0.94f_H$
System resonance frequency f_2	(a) $2.81f_H$ (b) $2.96f_H$ (c) $3.03f_H$	(a) $2.96f_H$ (b) $3.11f_H$ (c) $3.06f_H$	(a) $4.40f_H$ (b) $4.45f_H$ (c) $4.32f_H$	(a) $1.55f_H$ (b) $1.82f_H$ (c) $1.86f_H$	(a) $1.64f_H$ (b) $1.90f_H$ (c) $1.88f_H$	(a) $3.74f_H$ (b) $3.76f_H$ (c) $3.65f_H$
Maximum thermal efficiency $\eta_{T,max}$	64dB ($f = 0.36f_H$)	74dB ($f = 0.38f_H$)	81dB ($f = 0.83f_H$)	60dB ($f = 0.31f_H$)	66dB ($f = 0.36f_H$)	77dB ($f = 0.94f_H$)

By comparison, Gallas et al. [14] used their lumped parameter model to maximize the jet velocity magnitude at constant excitation voltage (U_n/e), without constraints for acoustic noise emission or input power. This is a different objective compared to the above approach which balances thermal efficiency and acoustic emission. Although not shown here, the model in this paper can reproduce the results by Gallas et al. [14]. This confirms their finding that two resonance frequencies f_1 and f_2 remain present in the overall system response, although the lower peak may be hidden due to strong nonlinear damping.

V. Conclusion

A general lumped parameter model has been derived for a synthetic jet actuator. The electromechanical dynamics are separated from the fluidic model $\rho c U_n / p_c$ since only a model relating cavity pressure to jet velocity minimizes external disturbances on the operating point (e.g. external pressure fields of adjacent synthetic jets, or variations in the actuator characteristics).

The overall system model has been validated against experimental data for a synthetic jet actuator, using measurements of the jet velocity, cavity pressure, diaphragm deflection, actuator voltage and current. The validation is performed for both a circular and rectangular sharp-edged orifice.

The agreement between model and experimental data is excellent up to a geometry-dependent limit frequency (Eq. (6)). Equation (24) is the most appropriate model to control the operation point of typical synthetic jet actuators, based on a measurement of the cavity pressure amplitude $|p_c|$:

$$|U_n| = \frac{|p_c|}{\rho c}\sqrt{\frac{2V_c}{A_n L_n'}}\frac{1}{\sqrt{\left(\frac{\omega}{\omega_H}\right)^2 + \sqrt{\left(\frac{\omega}{\omega_H}\right)^4 + K^2\left(\frac{V_c}{A_n L_n'}\right)^2\left(\frac{|p_c|}{\rho c^2}\right)^2}}}$$

This simple analytical model explicitly contains the effect of nonlinear nozzle damping, and has proven successful in controlling adjacent synthetic jet actuators [8,9]. The model requires two empirical coefficients K and β, which can be calibrated against a reference measurement of the jet orifice velocity. Alternatively, their values can be estimated based on theoretical values or correlations: (i) the damping coefficient K is comparable to the pressure loss coefficient for stationary flow through the nozzle [7]. (ii) The added fluid mass coefficient β can be estimated from the governing acoustic radiation impedance, which depends on the boundary conditions for the orifice.

For the configurations investigated here, these estimates of K (see Table 3) and β (see Table 1) are in reasonable agreement with the least-square fitted values (see Table 2). Considering the complex geometry and flow phenomena involved, deviations of only 13% for K and 30% for β are remarkable. This gives support to estimating the model parameters without a reference velocity measurement, yet for best accuracy, experimental validation as described in this paper is still recommended.

Although the validation experiments are performed using a loudspeaker-actuated synthetic jet, the model equations are provided for both electromagnetic and piezoelectric actuation. The difference in terms of the overall system response (i.e. electrical excitation to jet velocity) is discussed in Sect. IV. The response is characterized by two distinct resonance frequencies f_1 and f_2 determined by Eq. (26), which are related but not equal to the free diaphragm resonance and the Helmholtz frequency.

Even for an optimized actuator, two distinct resonance frequencies f_1 and f_2 remain present in the overall system response, although the lower peak may be hidden due to nonlinear damping [14]. Only the lower resonance peak is

affected by nozzle damping [17]. For an impinging synthetic jet actuator, the system model is used to formulate optimal design guidelines in terms of minimum acoustic emission and maximum thermal efficiency.

Two key contributions of this paper are (i) demonstrating how the nozzle flow dynamics affect the system response and in turn the optimal operating frequency and amplitude, and (ii) the characterization of the nozzle dynamics with two empirical parameters K and β which can be easily estimated or calibrated. This study has only considered synthetic jets issuing into a quiescent fluid. In cross-flow conditions, the model is expected to hold at least for moderate ratios of cross-flow to jet velocity magnitude, however this requires further validation. Future work should confirm the validity of the model for different orifice geometries, and provide a more detailed experimental verification of the effect on the thermal and acoustic efficiency for impinging synthetic jets.

Appendix A. Acoustic Radiation Impedance

The acoustic impedance ($Z = pA/U$) of a circular plate (diameter $2a = \sqrt{4A/\pi}$) oscillating in an infinite baffle has been derived analytically [23,24] as

$$Z = \rho c A\left(1 - \frac{J_1(2ka)}{ka} + j\frac{H_1(2ka)}{ka}\right) \tag{A1}$$

where the wave number $k = 2\pi f/c$, J_1 is a first order Bessel function of the first kind and H_1 is a first order Struve function [31]. A low frequency approximation ($ka < 0.5$) of Eq. (A1) is

$$Z^{(ka<0.5)} = \rho c A\left(\frac{1}{2}(ka)^2 + j\frac{8}{3\pi}ka\right) = \underbrace{-\frac{\rho A^2}{2\pi c}s^2}_{\text{real}} + \underbrace{\frac{8}{3\pi}\rho A\sqrt{\frac{A}{\pi}}s}_{\text{imaginary}} \tag{A2}$$

The exact impedance and its low frequency approximation are plotted in Fig. 12a. Tabulated values of the numerical solution for a rectangular plate oscillating in an infinite baffle are given by Burnett and Soroka [25] for aspect ratios of 1, 2, 4, 8, 16 and 32. Figure 12b shows the radiation impedance for an aspect ratio of 32:1, comparable to the 30:1 rectangular orifice used in this study.

At low frequency ($ka < 0.25$), Z is dominated by the reactance (dashed lines in Fig. 12):

$$Z^{(ka<0.25)} \cong \rho A\underbrace{\left(\beta\sqrt{\frac{4A}{\pi}}\right)}_{\substack{\beta \times \text{equivalent} \\ \text{diameter}}}s = M_f s \tag{A3}$$

where M_f represents a fluid mass adjacent to the surface. Table 1 lists values of β for some basic boundary conditions, yet in general the value is determined via calibration.

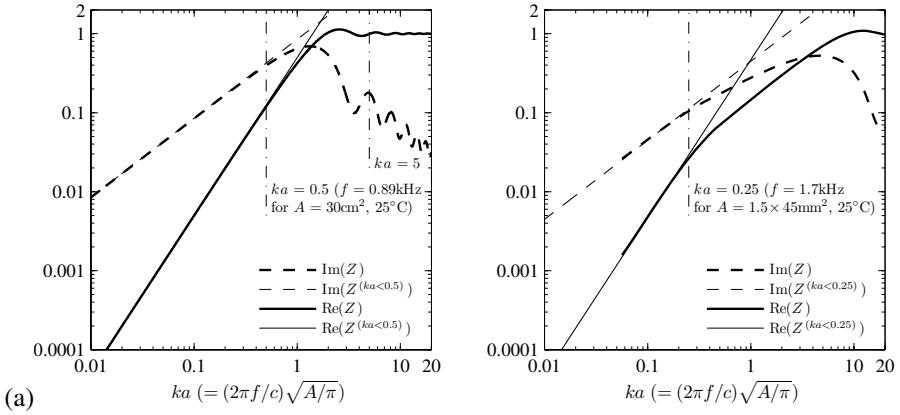

Fig. 12 Real (—) and imaginary (– –) parts of the acoustic radiation impedance *Z* for (a) a circular plate (Eqs. (A1, A2)) and (b) a rectangular plate of aspect ratio 32:1 in an infinite baffle (data from [24,25]).

Appendix B. Validation of the Loudspeaker Model

The modeling approach in Sect. II.B.1 can be validated against the manufacturer specifications for a given loudspeaker. A typical performance measure is the sound pressure level (SPL) at $r = 1$ m distance for an input power $P_e = 1$ W, or voltage $e = \sqrt{P_e Z_e}$. For omnidirectional radiation in one half-space, the pressure $p(r) = p(0)\sqrt{A_d / (2\pi r^2)}$. Based on the radiation impedance $Z_d = p(0) A_d / (x_d s)$,

$$p(r) = \sqrt{\frac{A_d}{2\pi r^2}} \frac{Z_d s}{A_d} \frac{x_d}{e} \sqrt{P_e Z_e} \quad \text{with } x_d/e \text{ and } Z_e \text{ according to [32]} \tag{B1}$$

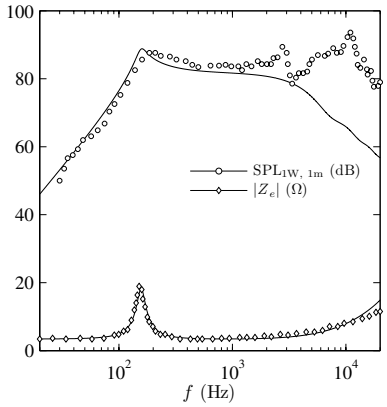

Fig. 13 Validation of model (lines) versus experimental data (markers) for a free mounted Visaton FR8 4Ω loudspeaker: (○) sound pressure level (SPL) in dB at *r* = 1m distance and P_e = 1W input power (Eq. (B1)) and (◇) electrical impedance Z_e (Eq. (14)).

Appendix C. Analytical Solution for the Nonlinear Transfer Function in Eq. (23)

The nonlinear transfer function in Eq. (23) can be rewritten as

$$\frac{\rho c U_n}{p_c} = \frac{\rho c A_n}{\rho A_n L_n' s + \dfrac{K A_n |p_c|}{2c} \left| \dfrac{\rho c U_n}{p_c} \right|} \tag{C1}$$

The absolute value in the denominator ensures the directionality of the damping force (Eq. (21)). Persoons and O'Donovan [7] substituted U_n and p_c by harmonic functions and approximated $|\sin\phi|\sin\phi \cong \sin\phi$. Instead, after defining $\xi = \rho c U_n / p_c$ Eq. (C1) becomes

$$\psi |\xi| \xi + j\Omega\xi + \chi = 0 \tag{C2}$$

where $\psi = \tfrac{1}{2} K A_n |p_c| / c$, $j\Omega = \rho A_n L_n' j\omega$ and $\chi = -\rho A_n c$. Substituting $\xi = |\xi|(\cos\phi + j\sin\phi)$ in Eq. (C2) and separating real and imaginary parts yields

$$|\xi| = \sqrt{\frac{2\chi^2}{\Omega^2 + \sqrt{\Omega^4 + 4\psi^2\chi^2}}} \text{ and } \phi = -\arctan\left(\frac{\Omega}{\psi|\xi|}\right) \tag{C3}$$

After back-substitution, this leads to the expression in Eq. (24).

Acknowledgments

Tim Persoons is a Marie Curie research fellow of the Irish Research Council for Science, Engineering and Technology (IRCSET). The experimental validation for this work was partly performed in the Cooling Technologies Research Center (CTRC) at Purdue University, West Lafayette IN, USA. The author gratefully acknowledges the support of Suresh V. Garimella and Darina B. Murray, and the assistance of Edgar Stone.

References

[1] Smith, B. L., and Glezer, A., "Jet vectoring using synthetic jets," *Journal of Fluid Mechanics*, Vol. 458, 2002, pp. 1-34. DOI: 10.1017/S0022112001007406

[2] Shuster, J. M., and Smith, D. R., "Experimental study of the formation and scaling of a round synthetic jet," *Physics of Fluids*, Vol. 19, No. 4, 2007, 045109. DOI: 10.1063/1.2711481

[3] Holman, R., Utturkar, Y., Mittal, R., Smith, B. L., and Cattafesta, L., "Formation criterion for synthetic jets," *AIAA Journal*, Vol. 43, No. 10, 2005, pp. 2110-2116.

[4] Fugal, S. R., Smith, B. L., and Spall, R. E., "Displacement amplitude scaling of a two-dimensional synthetic jet," *Physics of Fluids*, Vol. 17, No. 4, 2005, 045103. DOI: 10.1063/1.1872092

[5] Smith, B. L., and Swift, G. W., "Synthetic jets at large Reynolds number and comparison to continuous jets," *AIAA Paper* 2001-3030, 2001.

[6] Smith, B. L., and Glezer, A., "Vectoring of adjacent synthetic jets," *AIAA Journal*, Vol. 43, No. 10, 2005, pp. 2117-2124.

[7] Persoons, T., and O'Donovan, T. S., "A pressure-based estimate of synthetic jet velocity," *Physics of Fluids*, Vol. 19, No. 12, 2007, 128104. DOI: 10.1063/1.2823560

[8] Persoons, T., Farrelly, R., McGuinn, A., and Murray, D. B., "High dynamic range whole-field turbulence measurements in impinging synthetic jets for heat transfer applications," *Proceedings of the 15th International Symposium on Applications of Laser Techniques to Fluid Mechanics*, Lisbon, Portugal, 2010, No. 3.5.3-1710.

[9] Persoons, T., O'Donovan, T. S., and Murray, D. B., "Heat transfer in adjacent interacting impinging synthetic jets," *Proceedings of the ASME Summer Heat Transfer Conference*, 2009, No. HT2009-88440.

[10] Crittenden, T. M., and Glezer, A., "A high-speed, compressible synthetic jet," *Physics of Fluids*, Vol. 18, No. 1, 2006, 017107. DOI: 10.1063/1.2166451

[11] Lockerby, D. A., and Carpenter, P. W., "Modeling and design of microjet actuators," *AIAA Journal*, Vol. 42, No. 2, 2004, pp. 220-227.

[12] Rathnasingham, R. R., and Breuer, K. S., "Coupled fluid-structural characteristics of actuators for flow control," *AIAA Journal*, Vol. 35, No. 5, 1997, pp. 832-837.

[13] McCormick, D. C., "Boundary layer separation control with directed synthetic jets," *AIAA Paper* 2000-0519, 2000.

[14] Gallas, Q., Holman, R., Nishida, T., Carroll, B., Sheplak, M., and Cattafesta, L., "Lumped element modeling of piezoelectric-driven synthetic jet actuators," *AIAA Journal*, Vol. 41, No. 2, 2003, pp. 240-247.

[15] Oyarzun, M. A., and Cattafesta, L., "Design and optimization of piezoceramic zero-net mass-flux actuators," *AIAA Paper* 2010-4414, 2010.

[16] Kordik, J., Travnicek, Z., and Safarik, P., "Experiments on resonance frequencies of synthetic jet actuators," *Journal of Flow Visualization and Image Processing*, Vol. 17, No. 3, 2010, pp. 203-214.

[17] Kooijman, G., and Ouweltjes, O., "Finite difference time domain electroacoustic model for synthetic jet actuators including nonlinear flow resistance," *Journal of the Acoustical Society of America*, Vol. 125, No. 4, 2009, pp. 1911-1918. DOI: 10.1121/1.3081514

[18] Redionitis, O. K., Ko, J., and Kurdila, A. J., "Reduced order nonlinear Navier-Stokes models for synthetic jets," *Journal of Fluids Engineering-Transactions of the ASME*, Vol. 124, No. 2, 2002, pp. 433-443. DOI: 10.1115/1.1467598

[19] Yamaleev, N. K., and Carpenter, M. H., "Quasi-one-dimensional model for realistic three-dimensional synthetic jet actuators," *AIAA Journal*, Vol. 44, No. 2, 2006, pp. 208-216. DOI: 10.2514/1.14495

[20] Filz, C., Lee, D., Orkwis, P., and Turner, M., "Modeling of two dimensional directed synthetic jets using neural network-based deterministic source terms," *AIAA Paper* 2003-3456, 2003

[21] Kim, K., Beskok, A., and Jayasuriya, S., "Nonlinear system identification for the interaction of synthetic jets with a boundary layer," *Proceedings of the 2005 American Control Conference*, Vols. 1-7, 2005, pp. 1313-1318.

[22] Raju, R., Aram, E., Mittal, R., and Cattafesta, L., "Reduced-order models of zero-net mass-flux jets for large-scale flow control simulations," *AIAA Paper* 2010-4414, 2010.

[23] Pierce, A. D., *Acoustics: An Introduction to its Physical Principles and Applications*, Acoustical Society of America, New York, 1989, pp. 221-225.

[24] Beranek, L. L., *Acoustics*, Acoustical Society of America, New York, 1954, pp. 116-128.

[25] Burnett, D. S., and Soroka, W. W., "Tables of rectangular piston radiation impedance functions, with application to sound transmission loss through deep apertures," *Journal of the Acoustical Society of America*, Vol. 51, No. 5, 1972, pp. 1618-1623.

[26] Raju, R., Gallas, Q., Mittal, R., and Cattafesta, L., "Scaling of pressure drop for oscillatory flow through a slot," *Physics of Fluids*, Vol. 19, No. 7, 2007, 078107. DOI: 10.1063/1.2749814

[27] White, F. M., *Viscous Fluid Flow, 2nd Edition*, McGraw-Hill, New York, 1991, pp. 135-148.

[28] Silva, L. A., and Ortega, A., "Convective heat transfer due to an impinging synthetic jet: A numerical investigation of a canonical geometry," *Proceedings of the 12th IEEE Intersociety Conference on Thermal and Thermomechanical Phenomena in Electronic Systems*, IEEE, 2010.

[29] Persoons, T., McGuinn, A., and Murray, D. B., "A general correlation for the stagnation point Nusselt number of an axisymmetric impinging synthetic jet," *International Journal of Heat and Mass Transfer*, Vol. 54, Nos. 17-18, 2011, pp. 3900-3908. DOI: 10.1016/j.ijheatmasstransfer.2011.04.037

[30] Valiorgue, P., Persoons, T., McGuinn, A., and Murray, D. B., "Heat transfer mechanisms in an impinging synthetic jet for a small jet-to-surface spacing," *Experimental Thermal and Fluid Science*, Vol. 33, No. 4, 2009, pp. 597-603. DOI: 10.1016/j.expthermflusci.2008.12.006

[31] Aarts, R. M., and Janssen, A. J., "Approximation of the Struve function H1 occurring in impedance calculations," *Journal of the Acoustical Society of America*, Vol. 113, No. 5, 2003, pp. 2635-2637.

[32] Wiener, F. M., "On the relation between the sound fields radiated and diffracted by plane obstacles," *Journal of the Acoustical Society of America*, Vol. 23, No. 6, 1951, pp. 697-700.